Opto-magnonic Reservoir Computing Coupling Nonlinear Interfered Spin Wave and Visible Light Switching

Wataru Namiki[a,1], Yu Yamaguchi[a,b,1], Daiki Nishioka[a,b], Takashi Tsuchiya[a*], Kazuya Terabe[a]

a. National Institute for Materials Science, Research Center for Materials Nanoarchitectonics
1-1 Namiki, Tsukuba, Ibaraki, 315-0044, Japan
b. Tokyo University of Science, Faculty of Science
6-3-1 Niijuku, Katsushika, 125-8585, Japan
[1]Wataru Namiki and Yu Yamaguchi contribute equally to this work.
*E-mail: TSUCHIYA.Takashi@nims.go.jp

Keywords: (reservoir computing, spin wave, nonlinear interference, light switching)

Abstract

Physical reservoir computing is a promising approach to realize high-performance artificial intelligence systems utilizing physical devices. Recently, it has been experimentally found that nonlinear interfered spin wave multi-detection shows excellent performance for processing nonlinear time-series data due to its outstanding features: nonlinearity, short-term memory, and the ability to map in high dimensional space. However, said performance is considerably inferior to reservoir computing utilizing an optical circuit with a large volume. Herein, we develop reservoir computing with nonlinear interfered spin wave coupled with light switching, namely opto-magnonic reservoir computing. The spin wave was modulated through a crystal field transition that occurred in two different Fe^{3+} sites of $Y_3Fe_5O_{12}$ by visible light switching, and it was found that the spin wave modulated by visible light switching dramatically reduced normalized mean square errors to 4.96×10^{-3}, 0.163, and 3.66×10^{-5} for NARMA2, NARMA10, and second-order nonlinear dynamical equation tasks. Said excellent performance results from the strong nonlinearity caused by chaos and large memory capacity induced by reservoir states diversified by visible light switching.

1. Introduction

Reservoir computing is attracting attention as next-generation neuromorphic computing due to its lower computation cost and real-time operation for time-series data processing[[1],[2],[3]]. This is because the number of learning parameters in the reservoir computing model is much fewer than in a conventional deep learning model with a number of parameters. This advantage of reservoir computing arises from three key features: nonlinear transformation, the ability to map time-series data in higher

dimensional space, and short-term memory[4]. In recent years, physical reservoir computing, which is the reservoir computing utilizing a physical device as a reservoir, has been energetically studied to reduce information traffic on the network since processing data by physical reservoirs that can run on the terminal reduces the amount of extra data circulating on the network[[5]-[41]]. Candidates of such physical reservoirs are various devices, such as electrical circuits, electrochemical elements, spintronic devices, optical devices, robotic systems, ion-gating devices, and so on[[5]-[41]]. However, fatal issues of large electric power consumption, large dimensions, and slow operation speed are remained.

To overcome these issues, we reported that a nonlinear interfered spin wave muti-detection reservoir utilizing $Y_3Fe_5O_{12}$ (YIG) single crystal exhibits high computational performance for time-series data processing tasks [26]. This reservoir has some advantages: First, the spin wave reservoir can process the time-series data at a high operation speed corresponding to an optical circuit[26]. Second, spin wave propagation does not generate Joule heat. Third, a magnetic material has the advantage of miniaturization. In the previous study, this scheme was found to improve both nonlinearity due to spin wave interference and high dimensionality due to multi-detection of spin waves, compared with conventional spin wave reservoirs without both interference and multi-detection [26]. However, there is still room for improving computational performance. Reservoir computing utilizing spin wave interference has been attempted to improve performance by utilizing different physical conditions and arranging magnetic domain structures and signal detectors in some numerical studies[[18],[19],[20],[21]]. However, experimental demonstrations to improve computational performance have not yet been investigated. Utilizing spin wave manipulated by any external inputs is one of the effective methods to realize different physical conditions of magnetic material and to implement a practical physical reservoir with high computational performance and small volume.

In this study, we developed a high-performance reservoir computing device using the nonlinear interfered spin wave multi-detection coupled with light irradiation to realize different physical conditions. This is the first experimental study about an application of interaction between nonlinear interfered spin wave and visible light irradiation to the physical reservoir computing to improve the expression power of the reservoir through introducing multiple reservoirs with reservoir states varied by spin wave manipulation. A ferrimagnetic insulator YIG single crystal was used as a functional spin waveguide in this study since it is known that visible light irradiation changes the spin configuration of the YIG from the ground state to the excitation state. It can be expected that this change may affect spin wave property through modulated saturation magnetization and magnetic anisotropy[[42],[43],[44]]. Thus, the presence or absence of visible light irradiation (i.e., visible light switching) can be used to improve the ability to map time series data in higher dimensional space of reservoir since spin wave variation modulated by the irradiation in a single magnetic material can be dealt as virtually multiplied reservoir.

2. Experimental methods

2.1. Fabrication of a device for reservoir computing utilizing interfered spin wave

A side polished YIG single crystal with 111 orientation was supplied by MTI Co. (USA). The diameter and thickness of the single crystal were 5 mm and 0.5 mm, respectively. Coplanar waveguides comprised a 10 μm wide signal line and two 20 μm wide ground lines. 10 nm-thick Ti and 90 nm-thick Au were continuously deposited by electron beam evaporator. The distance between the edges of the antennas was 30 μm. The previous work describes the details of the device and the characteristic dimensions of the device[26].

2.2. Experimental setup for spin wave detection

All experiments were performed in a high-frequency signal measurement system, consisting of rf probes and an electromagnet, which was made by Toei Scientific Industrial Co., Ltd. An external magnetic field was applied perpendicular to the sample surface. The sample was kept at 295 ± 1 K. The exciters and detectors shown in Fig. 1(a) were connected, through rf probes, to an arbitrary waveform generator and a mixed signal digital oscilloscope, respectively. Pulse voltage was input to the exciter to excite the spin waves. Rise and fall times and the pulse-on time were 320 ps. The input and output signals were amplified to 30 dB and 38 dB, respectively. To avoid detection of excess spin waves excited by previous sequences, long 4 μs intervals were inserted between each sequence. An average of 500 waveforms were taken to improve the signal-to-noise ratio (S/N). A solar simulator, HAL-320 (Asahi Spectra Co.), was used as a light source to irradiate visible light. The spectrum of the light source was shown in Fig. 1(c). Measurements under the conditions with visible light irradiation (‘Light’ state) and without visible light irradiation (‘Dark' state) were performed separately. The light is completely blocked except for the light source used.

2.3. Nonlinear time series data prediction task

The subject reservoir computing system was trained and tested with a random waveform to predict the output from a NARMA model. To input to a reservoir computing system, the original random waveform $u(k)$ = [0,0.5], with a time step of 5000, is transformed to pulsed waveforms with rise and fall times of 360 ps, a pulse-on time of 0 ps, and various intervals of 2 ns – 20 ns. Pulsed waveforms, with a maximum value of 400 mV, are applied to Exciter A and/or Exciter B. The voltages induced by a spin wave, which reaches each detector, are acquired by an oscilloscope, and 50 virtual nodes per detector are from each induced voltage. 50 reservoir states (w/o multi-detection) or 100 reservoir states (with multi-detection) are obtained from 1D input $u(k)$ transformed nonlinearly by the reservoir as the conditions ‘Light’ and ‘Dark’. 25 reservoir states (w/o multi-detection) or 50 reservoir states (with multi-detection) are obtained from the input $u(k)$ transformed nonlinearly by the reservoir

on the conditions ‘Light’ and ‘Dark’ and combined to make 50 reservoir states (w/o multi-detection) or 100 reservoir states (with multi-detection) as the condition ‘Mix’. Time steps are separated into training phases with a time step of 3500 and test phases with a time step of 500 after the first time step of 1000 is discarded.

2.4. Micromagnetic simulation

We performed a theoretical simulation using a Mumax3 micromagnetic simulator[45]. YIG with 380 μm × 90 μm × 0.12 μm is used to investigate the spin dynamics near a surface region in the vicinity of an antenna. The two exciters used is consisted of a signal line (10 μm × 90 μm × 0.12 μm) and two ground lines (20 μm × 90 μm × 0.12 μm). The detection areas of the two detectors are 10 μm × 90 μm × 0.12 μm, which corresponds to the signal lines of the detectors. The mesh was cubic, measuring 40 nm × 40 nm × 40 nm along the Cartesian coordinates defined by the origin at the center of the surface plane on the YIG. A spin was located at every mesh corner. The simulation time step was 10 ps. To simulate spin wave property variation at various conditions, these material parameters were set to various values corresponding to the experimental result of magnetization measurement. A cubic magneto-crystalline anisotropy of 0.0, an exchange stiffness constant of 3.7 pJ/m, and a damping constant of 1×10^{-4}. A static magnetic field of 0.3 T is applied along the z-axis (i.e., perpendicular to the YIG surface) over the entire region. A maximum excitation field with a rectangular shape-pulse is set at 80 mT, which is estimated from a simulation result shown in the literature[46], along the y-axis at the exciters applied in the exciter. The field vectors at the signal and ground lines are positive and negative since electric current flows in the opposite direction.

3. Results and Discussion

3.1. Spin wave modulation by visible light irradiation

Four coplanar waveguides for two input (Exciter A and Exciter B) and two output (Detector A and Detector B) antennas were deposited on (111) of the YIG single crystal substrate. Two input antennas and two output antennas are connected to an arbitrary waveform generator and an oscilloscope, respectively, as shown in Fig. 1(a). A vector network analyzer is used for the transmission characteristic of the spin wave from Exciter A (Ex. A) to Detector A (Det. A). Visible light irradiation is switched to 'On’ (‘Light’) and ‘Off’ (‘Dark’) states. Details of measurement configuration are described in the Methods section. Fig. 1(b) shows a cross-sectional transmission electron microscope (TEM) image and a selected area electron diffraction (SAED) of the YIG single crystal. It was confirmed that YIG shows highly crystalline along 111 in out-of-plane and in-plane directions. Lattice constants along [001] and [110] measured from SAED were 1.2715 nm and 1.7762 nm, which are in good agreement with the reported values[47]. A light source of visible light irradiation used in this

study has a broad spectrum ranging from 1 to 4 e V, as shown in Fig. 1(c). YIG possesses two Fe sites located at the centers of oxygen octahedrons and tetrahedrons in the crystal, and it is known that the Fe sites emerging crystal field transition are different depending on the incident energy[[42],[43],[44]. A reflectance spectrum reflects the information about Fe^{3+} crystal field transition in a YIG, and a measured spectrum is shown in the lower panel of Fig. 1(c). The feature at the region above 2 eV is in good agreement with reported spectra, which indicate $^6A_1$ (high spin) → $^4T_1$ (low spin) tetrahedral Fe^{3+} crystal field transition[[42],[44]]. Also, an increment tendency observed at the region above ~3 eV and absorption edges at the ~2.8, ~3.4, and ~4.5 eV in the absorption spectrum are in good agreement with the reported one, showing charge transfer excitation from 2p → 3d[44]. However, no information was obtained in lower energy regions below 2.0 eV since the significant structure was not confirmed in a reflectance measurement. Thus, we measured a transmittance spectrum to obtain an absorption spectrum at the lower energy region. From this measurement, the peak indicating $^6A_{1g}$ (high spin) → $^4T_{1g}$ (low spin) octahedral Fe^{3+} crystal field transition was found at 1.4 eV[42]. Thus, a used light source occurs the crystal field transition in two different Fe^{3+} sites of YIG, and spin wave property is modulated by visible light switching through magnetization and/or magnetic anisotropy, which are sensitive to spin configuration near fermi energy. Figure 1(d) shows the spin wave signal at the time domain under the 'Light' and 'Dark' conditions. Pulse signal with pulse width, rise, and fall times of 320 ps is input to Ex. A and spin wave signal is detected at Det. A. It was found that the waveform is changed by visible light irradiation at the entire time domain, and the maximum difference between the two signals is approximately 8 mV. Visible light contributes to only spin wave modulation since the amplitude at the gray region, which indicates crosstalk induced by pulsed input, is not changed. This modulation can be found in waveforms at various input voltage and magnetic field conditions, as shown in Fig. 1(e). The difference between two waveforms under 'Light' and 'Dark' is larger at higher input voltage compared to lower input voltage. If the phases of two waveforms do not match, the difference between those looks larger since the difference is calculated from the normalized area of the subtraction of two waveforms. To reveal the origin of modulation by visible light irradiation, we measured the magnetic field dependence of spin wave resonance frequency under two conditions (i.e., 'Light' and 'Dark'). The spin wave frequency, under the application of a perpendicular magnetic field, is described as follows;

$$f = \gamma \sqrt{(H - H_a)\left\{(H - H_a) + M_S\left(1 - \frac{1 - e^{-wd}}{wd}\right)\right\}} \qquad (1),$$

where f, γ, H, H_a, M_S, w, and d are frequency, gyromagnetic ratio, applied external field, magnetic anisotropy field, saturation magnetization, wavenumber of spin wave, and YIG thickness, respectively. Here, γ and M_S were set at 2.8 MHz/Oe and 1984 Gauss[26], which were obtained from the magnetization measurement, at the dark condition. Transmitted spin wave signals under two

conditions are shown as white lines in Figs. 1(f) and (g), while some horizontal lines do not result from spin waves but from background signals from the measurement circuit. Fitting results for M and H_a are summarized in Fig. 1(h). M_S of 1984 Gauss and H_a of 147.8 mT under the condition 'Dark' was reduced to 1846.3 Gauss and 142.6 mT, respectively, by light irradiation. These modulations result from a change in the spin configuration of the Fe site in YIG, as discussed in Fig. 1(c). Visible light irradiation leads to a transition from the ground high spin state ($S = 5/2$) to the excitation low spin state ($S = 3/2$), where S denotes the spin angular momentum of the Fe ion[42]. This transition is selectively induced by two wavelength regions: the shorter wavelength region (400 -700 nm) and longer wavelength region (800 – 1000 nm) affect Fe^{3+} ions at the center of tetrahedron and octahedron, respectively[42]. Both transitions occurred in the case of visible light irradiation utilized in this study and led to a reduction of M_S. Also, H_a was reduced by spin-orbit interaction with spin state transition. These magnetic property variation affects spin wave frequency, as described in Eq. (1). Figure 1(i) shows spin wave transmission spectra measured under the conditions 'Dark' and 'Light'. It was found that spin wave frequency was shifted to 17.6 MHz higher frequency region by the light switching from 'Dark' to 'Light'. This shift results from an increase in the effective magnetic field ($H–H_a$) with a decrease in H_a. Here, it was confirmed that there was only a little temperature change with a slight slope of approximately 3.6 °C/2500 seconds on the YIG surface by monitoring the temperature with a thermocouple, as shown in Fig. 1(j). According to the literature, the magnetization of YIG gently decreases 0.12 %·μ_B/°C, where μ_B denotes Bohr magneton, by heating near room temperature[48]. The rate of magnetization changed by light switching in our study was approximately -7 %, which is equivalent to quite a large temperature variation to as high as 58 °C by assuming the heating-induced magnetization variation mechanism. As the assumption is completely inconsistent with the quite small temperature variation of 3.6 °C observed in the experiment, the spin wave modulation discussed above did not result from any heat effect but from a light switching.

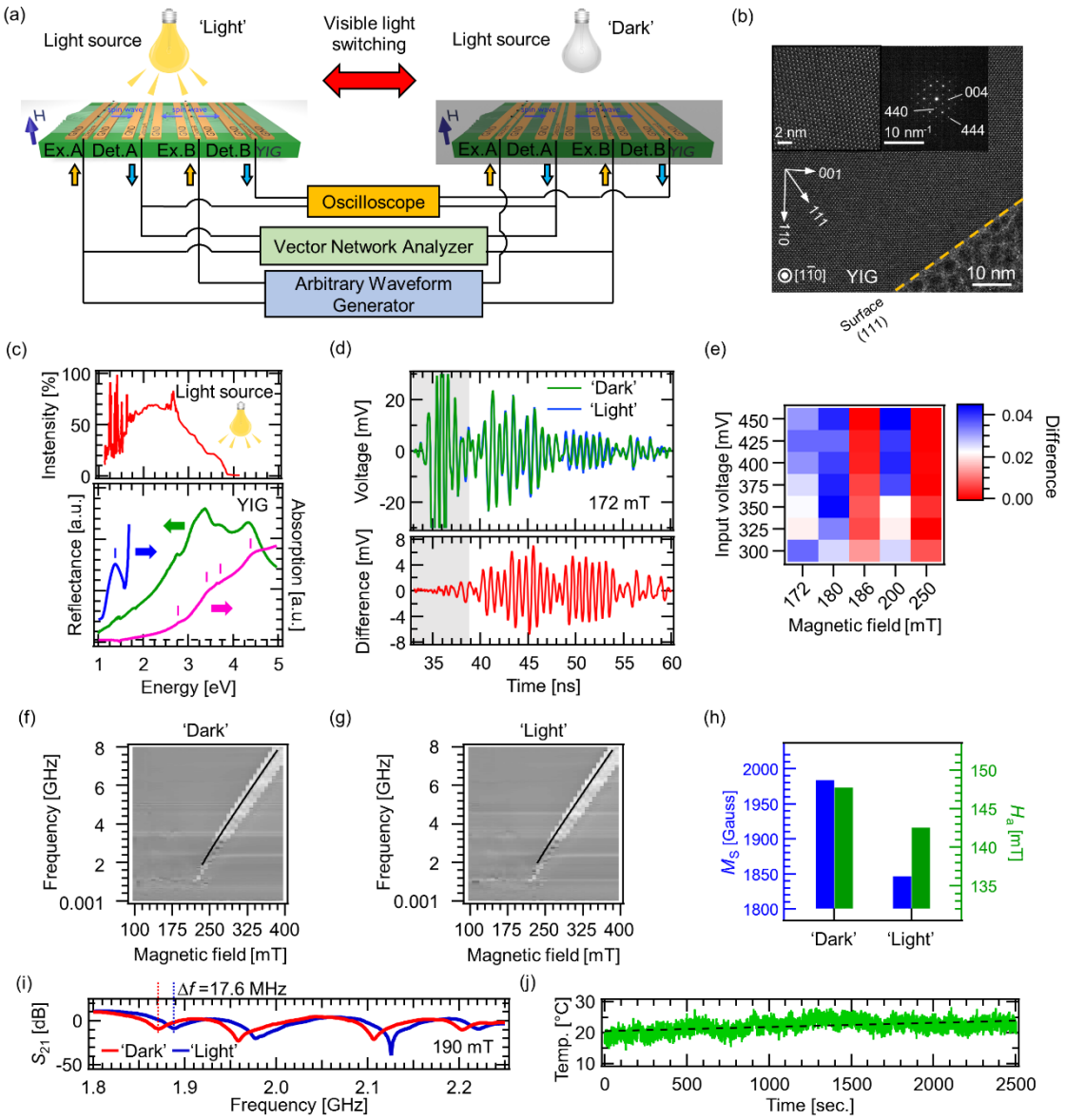

Fig. 1. (a) measurement configuration of an opto-magnonic device. An arbitrary waveform generator is connected to Exciter A (Ex. A) and Exciter B (Ex. B). A vector network analyzer is connected to Ex. A and Detector A (Det. A). An oscilloscope is connected to Det. A and Detector B (Det. B). (b) TEM image of a cross-section of the $Y_3Fe_5O_{12}$ (YIG) single crystal and its selected area electron diffraction image. (c) (upper) spectrum of a light source and (lower) reflectance and absorption spectra of the YIG single crystal. (d) (upper) spin wave signals at the time domain under the conditions with light off ('Dark') and light on ('Light') and (lower) subtraction between two spin wave signals shown in the upper panel. (e) Intensity change of amplitude of difference between spin wave signals under the conditions with light off and light on. (f) Magnetic field dependence of spin wave frequency under the condition of 'Dark'. (g) Magnetic field dependence of spin wave frequency under the condition of 'Light'. (h) Saturated magnetization M_S and anisotropic magnetic field H_a variations of the YIG single crystal at various conditions 'Dark' and 'Light'. (i) Spin wave transmission

spectra at 190 mT under the conditions 'Dark' (red solid line) and 'Light' (blue solid line). (j) Time dependence of surface temperature on the YIG single crystal. Temperature was measured as electromotive force using a K thermocouple attached to the surface.

3.2. Reservoir computing with opto-magnonic reservoir device

Figure 2(a) shows the schematic concept of physical reservoir computing utilizing spin wave and visible light switching. Although the basic concept is similar to nonlinear interfered spin wave multi-detection in the previous study[26], this study has a unique feature in that two reservoirs are virtually generated by two conditions (i.e., light and dark). Figure 2(b) shows the spin wave response, which is detected at Detector A, at first and second time step k (i.e., k =1 and k =2) when a random pulsed train was inputted under the conditions of 'Light' and 'Dark'. Colored plots denote the value of each node, and it can be seen that these values are changed by visible light irradiation. This result contributes to the improvement of the variety of reservoir states. Figure 2(c) shows the spin wave response, which is detected at Detector B, at k =1 and k = 2 when the random pulsed train was inputted under the conditions of 'Light' and 'Dark'. By comparison with Figs. 2(b) and (c), one can see that the detecting position changes the spin wave signal, and this difference improves the expression power of the reservoir, as reported in the previous study[26]. Spin wave signals detected at Detector B are also sensitive to irradiation. Therefore, in addition to spin wave multi-detection, visible light switching also significantly improves the high dimensionality of the reservoir. To obtain the node state variation at various time steps k, 50 nodes per k are taken from each detected signal. Figures 2(d) and (e) show 50 node states obtained from Det. A and Det. B at the condition under light and dark, respectively. The multi-detection and visible light switching give variation to the reservoir state. Here, we combine these node states as follows: (i) three reservoir states with 50 node states taken from Det. A at the conditions under 'Light', 'Dark', and 'Mix', which is condition mixing 'Light' and 'Dark'. Here, the reservoir state at the condition under 'Mix' is generated by taking 50 nodes from Det. A at the conditions under 'Light' (25 nodes) and 'Dark' (25 nodes). (ii) three reservoir states with 100 nodes taken from Det. A and Det. B at the conditions under 'Light', 'Dark', and 'Mix'. Here, the reservoir state with 100 nodes taken from Det. A at the condition under 'Light' (25 nodes) and 'Dark' (25 nodes) and Det. B at the condition under 'Light' (25 nodes) and 'Dark' (25 nodes). Figure 2(f) shows the schematic process flow for time series data processing tasks so as to evaluate the nonlinear transform function of a reservoir system. Here, the second-order nonlinear dynamic equation task and nonlinear autoregressive moving average (NARMA) task are adopted for the evaluation[7,13,26,37,38]. In the case of a second-order nonlinear dynamical equation task, a random wave is input to a second-order nonlinear dynamical system in solving a second-order nonlinear dynamical equation task. The output $d(k)$ from this dynamical system at k is described as follows;

$$d(k) = 0.4d(k-1) + 0.4d(k-1)d(k-2) + 0.6u^3(k) + 0.1. \quad (2)$$

$d(k)$ depends not only on the current input $u(k)$ but also on the past two states $d(k\text{-}1)$ and $d(k\text{-}2)$ at discrete times k-1 and k-2. The second term on the right-hand side of the equation is the cross term that makes it a second-order nonlinear system. In the case of the NARMA task, a random wave is input to a NARMA2 and NARMA10, which require short-term memory from the previous 2 and 10 steps, respectively, as defined below[49];

$$d(k+1) = 0.4d(k) + 0.4d(k)d(k-1) + 0.6u^3(k) + 0.1 \quad (3)$$

and

$$d(k+1) = 0.3d(k) + 0.05d(k)\sum_{m=0}^{9} d(k-m) + 1.5u(k)u(k-9) + 0.1. \quad (4)$$

Before input to the reservoir system, the original random wave is processed to the pulsed signal at intervals of 2, 5, 10, 15, and 20 ns as pre-processing. Each input of these signals is sent to a reservoir computing system to which perpendicular magnetic fields of 172, 180, 186, 200, and 250 mT are being applied. 100 node states of the reservoir are generated by the means described above. A reservoir output $y(k)$ is described below;

$$y(k) = \sum_{i=1}^{n} W_i X_i(k) + b. \quad (5)$$

Here, n and b are the total number of nodes and a bias term, respectively[26,37,38]. W_i is optimized by ridge regression as training for the system to minimize the difference between the target waveform output $d(k)$ from the theoretical model and the reservoir output $y(k)$[26]. To compare the performance of the reservoir system with that of other systems, a normalized mean square error (NMSE) is introduced as follows,

$$\mathrm{NMSE} = \sum_{k=1}^{T} \frac{(d(k)-y(k))^2}{(d(k))^2}. \quad (6)$$

Here, T is the length of the training phase (T = 3500) or test phase (T = 500). NMSE for NARMA tasks is described as follows;

$$\mathrm{NMSE}_{\mathrm{var}} = \frac{\sum_{k=1}^{T}(d(k)-y(k))^2}{\sum_{k=1}^{T}(d(k)-d_{\mathrm{ave.}})^2} \quad (7)$$

where $d_{\mathrm{ave.}}$ is the time average of $d(k)$.

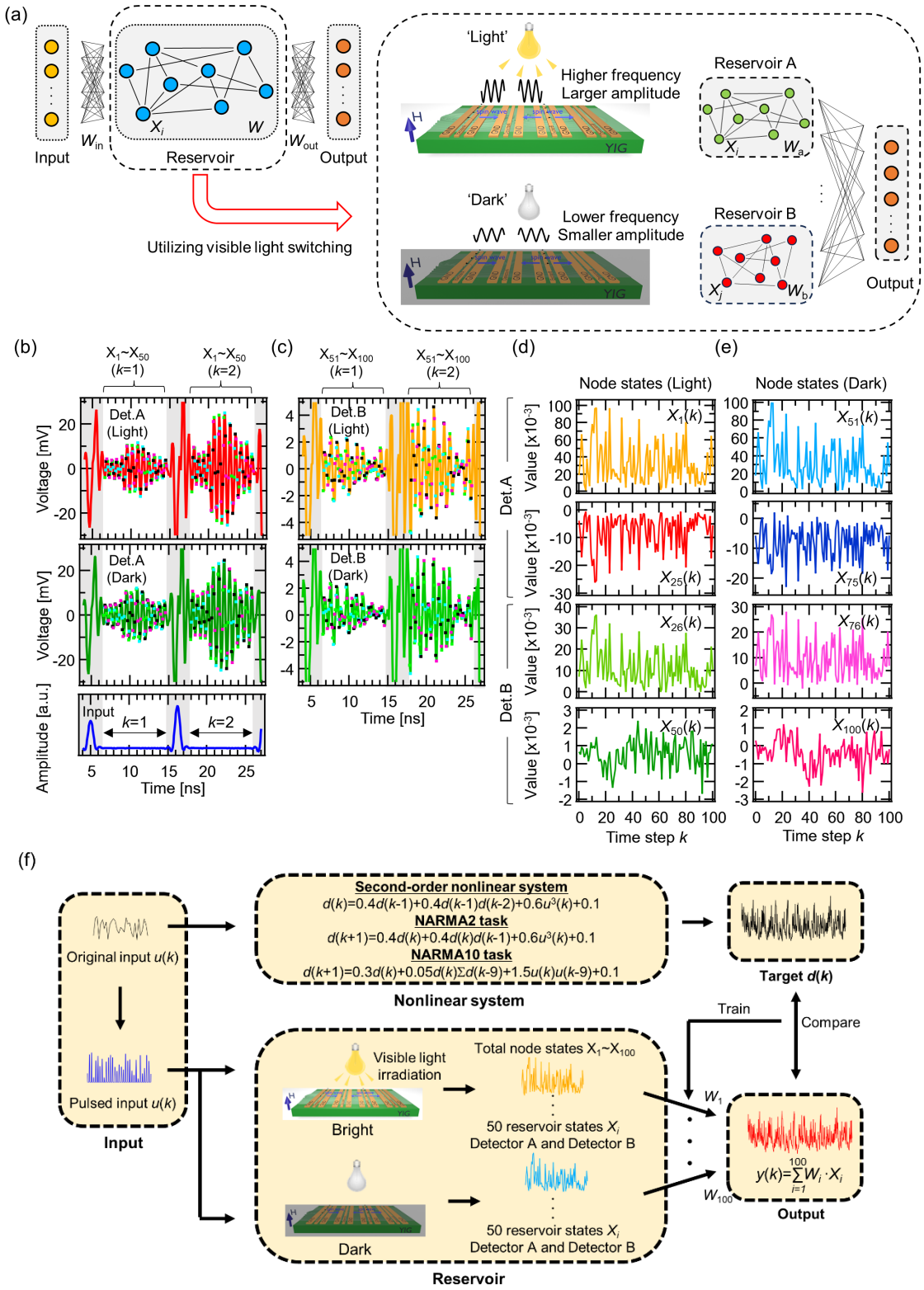

Fig. 2. (a) General concept of an opto-magnonic reservoir computing. (b) (Upper) A cropped signal detected at Detector A under the condition 'Light'. (Middle) A cropped signal detected at Detector A under the condition

'Dark'. (Lower) A cropped input random waveform. The gray region is the crosstalk region induced by input pulse voltage. (c) (Upper) A cropped signal detected at Detector B under the condition 'Light'. (Lower) A cropped signal detected at Detector B under the condition 'Dark'. Light green, light blue, black, and purple squares denote node states of $X_{4n+1}(k)$, $X_{4n+2}(k)$, $X_{4n+3}(k)$, and $X_{4n+4}(k)$ taken from the detected signal. (d) Node states of $X_1(k)$, $X_{25}(k)$, $X_{26}(k)$, and $X_{50}(k)$ under the condition 'Light'. $X_1(k)$ to $X_{25}(k)$ and $X_{26}(k)$ to $X_{50}(k)$ are taken from signals detected at Detector A and Detector B, respectively. (e) Node states of $X_{51}(k)$, $X_{75}(k)$, $X_{76}(k)$, and $X_{100}(k)$ taken from signal measured under the condition 'Dark'. $X_{51}(k)$ to $X_{75}(k)$ and $X_{76}(k)$ to $X_{100}(k)$ are taken from signals detected at Detector A and Detector B, respectively. (f) General concept process flow diagram of a time-series data processing task using a reservoir computing system with the opto-magnonic device.

3.3. Evaluation of the physical reservoir performance for time-series data prediction tasks

Figure 3(a) shows the comparison of target and prediction waveforms from the second-order nonlinear system and reservoir system, respectively, in the test phase. An output waveform of the physical reservoir was in good agreement with a target waveform, and the NMSE was 3.66×10^{-5}. Figure 3(b) shows NMSE changes at various pulse intervals and magnetic fields. NMSE is lower in lower magnetic fields of 172 ~ 186 mT and at shorter intervals of 5 and 10 ns. This tendency can be seen in the comparison shown in every three panels for 'Dark', 'Light', and 'Mix'. The lowest NMSEs in the case of 'Dark' and 'Light' are 5.14×10^{-5} and 5.86×10^{-5}, respectively. Then, the NMSE changes drastically in the case of 'Mix, ' and the lowest NMSE drops to 3.66×10^{-5}. This value is much lower than the values from any other physical reservoir computing systems that have been reported, in which the NMSEs of a theoretical reservoir computing system with 24 spin torque oscillators were ~1.31×10^{-3}[13], an experimental reservoir computing system with 90 metal-oxide memristors were ~3.13×10^{-5}[7], electric double layer and redox-based ion-gating reservoir were 2.1×10^{-4} and 5.1×10^{-4}[37,38], and nonlinear interfered spin wave multi-detection was 8.37×10^{-5}[26], respectively. Next, NARMA tasks were performed to evaluate the ability to predict dynamic systems with the short-term memory of the physical reservoir[5,47]. The compared results of target and prediction waveforms from NARMA2 and NARMA10 systems and reservoir system, respectively, in the test phase, as shown in Figs. 3(c) and (e). Output waveforms of the physical reservoir were in good agreement with respective target waveforms and $NMSEs_{var.}$ were 4.96×10^{-3} and 0.163 for NARMA2 and NARMA10. Figures 3(d) and (f) show $NMSEs_{var.}$ changes at various intervals and magnetic fields. The condition dependence of $NMSE_{var.}$ for NARMA2 is in good agreement with NMSE variation for second-order nonlinear system equation, while the condition dependence of that for NARMA10 differs from those. For NARMA2 task, the $NMSE_{var.}$ is lower in weaker magnetic fields and at shorter pulse intervals, as in the second-order nonlinear system equation task. On the other hand, the $NMSE_{var.}$ is lower in the

middle magnetic field of 180 and 186 mT and at relatively longer pulse intervals of 15 ns and 20 ns for the NARMA10 task. This result shows that the conditions for tasks that require mainly nonlinearity and short-term memory, which can be optimized by magnetic field and pulse interval[26]. Furthermore, it was found that visible light irradiation deteriorates the performance, meaning that the $NMSE_{var.}$ under the condition 'Light' is larger than that under the condition 'Dark', in the case of utilizing the reservoir under only one condition. This experimental fact may result from the fact that spin configuration modulation induced by the optical effect shown in Fig. 1(c) contributes to the change of nonlinearity and/or short-term memory of the reservoir. In any case, the $NMSEs_{var.}$ in both tasks were reduced by adopting the condition 'Mix', and the lowest $NMSE_{var.}$ reaches to 4.96×10^{-3} for NARMA2 and 0.163 for NARMA10. Updated benchmarks for NARMA2 and NARMA10 are summarized in Figs. 3(g) and (h), respectively. The reservoir performance for NARMA2 is the best in physical reservoir devices. The performance for NARMA10 is superior to most experimental reservoir devices reported to date[[27],[30],[31],[32],[39],[41]], except for some reservoir devices with larger device volumes[[5],[6],[33],[34]], and improving the performance of the reservoir device utilizing nonlinear interfered spin wave multi-detection was succeeded by adopting visible light switching.

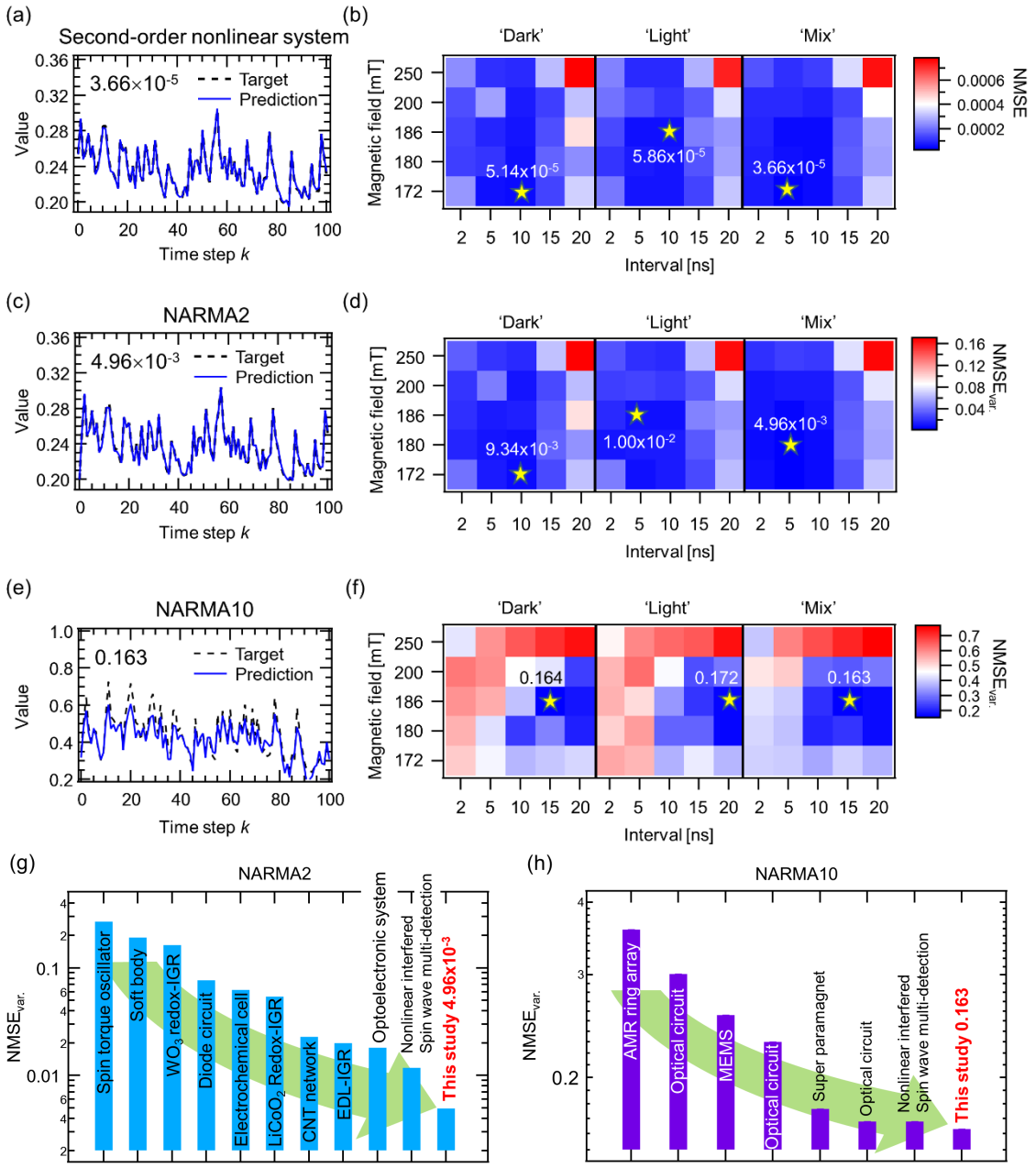

Fig. 3. (a) Compared result of outputs from the opto-magnonic reservoir and a second-order nonlinear system at the testing phase. The black dashed and blue solid lines denote the target waveform and prediction results, respectively. (b) NMSE variation for prediction of a second-order nonlinear system at various magnetic fields and pulse intervals. (left) Multi-detection with interference under the condition 'Dark'. (middle) Multi-detection with interference under the condition 'Light'. (right) Multi-detection with interference under the condition 'Mix'. (c) Compared results of outputs from the opto-magnonic reservoir and a NARMA2 system at the testing phase. The black dashed and blue solid lines denote the target waveform and prediction results,

respectively. (d) $NMSE_{var.}$ variation for predicting a NARMA2 system at various magnetic fields and pulse intervals. (left) Multi-detection with interference under the condition 'Dark'. (middle) Multi-detection with interference under the condition 'Light'. (right) Multi-detection with interference under the condition 'Mix'. (e) Compared results of outputs from the opto-magnonic reservoir and a NARMA10 system at the testing phase. The black dashed and blue solid lines denote the target waveform and prediction results, respectively. (f) $NMSE_{var.}$ variation for predicting a NARMA10 system at various magnetic fields and pulse intervals. (left) Multi-detection with interference under the condition 'Dark'. (middle) Multi-detection with interference under the condition 'Light'. (right) Multi-detection with interference under the condition 'Mix'. (g) Comparison of $NMSEs_{var.}$ of various devices on NARMA2 task. The $NMSEs_{var.}$ of a spin torque oscillator[14], soft body[35], redox-ion gating reservoir (IGR)[38], diode circuit[10], electrochemical cell[9], carbon nanotube (CNT) network[11], electric double layer (EDL)-IGR[37], optoelectronic system[50], and nonlinear interfered spin wave multi-detection[26] are also shown. (h) Comparison of $NMSEs_{var.}$ of various devices on NARMA10 task. The $NMSEs_{var.}$ of anisotropic magnetoresistance (AMR) ring array[27], optical circuits[[30],[31],[32]], micro electromechanical system (MEMS)[39], super paramagnet[41], nonlinear interfered spin wave multi-detection[26] are also shown.

3.4. Short-term memory evaluation of the physical reservoir

To evaluate a short-term memory property of the reservoir device, we performed a short-term memory task that measures how the system can reconstruct past input data as current output[26]. The square of the correlation coefficient r (i.e., determination coefficient r^2) between the ideal targets and the model predictions is determined by utilizing the relationship described as follows:

$$r^2(\tau) = \frac{Cov(u(k-\tau),y(k,\tau))^2}{Var(u(k-\tau))Var(y(k,\tau))}. \qquad (8)$$

Here, Cov(A, B) is the covariance between vectors A and B, and Var(A) ≅ Cov(A, A), and $u(k\text{-}\tau)$ denotes a time series data delayed time step of k. r^2 takes values between 0 and 1, where the value of 1 indicates perfect replication of the targets. The short-term memory capacity C_{STM} is then calculated by taking the sum of $r^2(\tau)$ over the range of delays. C_{STM} is defined as follows,

$$C_{STM} = \sum_{\tau=1}^{\infty} r^2(\tau). \qquad (9)$$

Figure 4(a) shows step delay τ dependence of determination coefficient $r^2(\tau)$ (i.e., forgetting curves) at three conditions of 'Dark', 'Light', and 'Mix'. The ability for prediction decreases as the step delay τ increases. τ at the intersection of the forgetting curve and the dashed line with $r^2(\tau)$ of 0.5 becomes larger for 'Dark', 'Light', and 'Mix', in that order. The reservoir with each condition 'Dark', 'Light', and 'Mix' can reproduce the state at past 26, 28, and 31 steps, respectively, and it was found that the short-term memory property that the physical device possesses is enough to predict NARMA10, which requires the past state below 10. This result is a reason why this reservoir can precisely predict

NARMA10. Memory capacity (MC) is an indicator for short-term memory evaluation. The reservoir has a good short-term memory when MC shows a large value. MC is defined as the area under the forgetting curves, as summarized in Fig. 4(b), and the short-term memory is enhanced with increasing MC. MC improves at the region above a magnetic field of 180 mT and an interval length of 10 ns under all three conditions. MC of the best condition for NARMA10 are 24.01 for 'Dark', 28.01 for 'Light', and 32.08 for 'Mix'. However, there is no relationship between MC and $NMSE_{var.}$ for NARMA10. While the largest MC for 'Mix' leads obviously to the reduction of $NMSE_{var.}$, $NMSE_{var.}$ of 0.164 at 'Dark' with a relatively small MC of 24.01 close to that of 0.163 at 'Mix'. Thus, although it was found that visible light irradiation leads to MC enhancement in this short-term memory evaluation, the origin of high prediction performance cannot be explained solely on the basis of MC. Therefore, we investigated another important property: nonlinearity, as discussed in the following section.

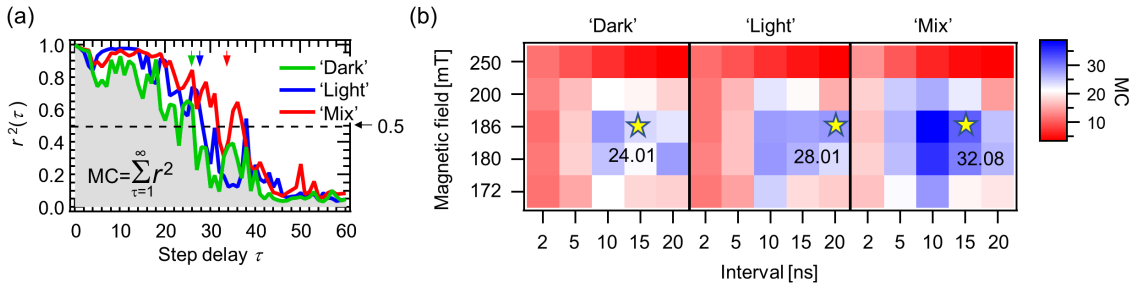

Fig. 4. (a) Forgetting curve described by determination coefficient r^2 variation at step delay τ. Light green, blue, and red lines denote the forgetting curve of the reservoir device under the conditions 'Dark', 'Light', and 'Mix', respectively. A dashed line denotes r^2 of 0.5. (b) Memory capacity (MC) variations at various magnetic fields and pulse intervals. Multi-detection with interference under the conditions (left) 'Dark', (middle) 'Light', and (right) 'Mix'.

3.5. Nonlinearity evaluation of the physical reservoir

Nonlinearity is also quite important for the reservoir, as well as short-term memory[[2],[4]-[27],[29]-[41]]. Lyapunov exponent λ is an indicator of the nonlinearity of complex systems, including physical reservoir[51], and maximum Lyapunov exponents λ_{max} were calculated by the Jacob matrix method[52] to evaluate the nonlinearity of the reservoir system. λ_{max} is generally used to determine if the response of a dynamical system is orderly or disorderly (i.e., chaotic); when λ_{max} is negative (positive), the system is orderly (disorderly). Furthermore, the degree of nonlinearity of the system improves as λ_{max} increases[26]. Figure 5(a) shows an example of a Lyapunov spectrum analyzed using the reservoir state at the best condition for NARMA10 of 'Dark'. The Lyapunov exponents show various values ranging from approximately -2.8 to approximately 1.4. Thus, λ_{max} is 1.39 under this condition. All λ_{max}s are summarized in Fig. 5(b). Under both conditions 'Dark' and 'Light', λ_{max} shows

a relatively small (large) value at the condition of pulse interval below 10 ns (above 15 ns). λ_{max} at the best condition for NARMA10 shows 1.39 and 1.04 for 'Dark' and 'Light', respectively, (i.e., λ_{max} of 'Dark' > λ_{max} of 'Light'). This relation shows that the nonlinearity at the best condition with 'Dark' is stronger than the nonlinearity at the best condition with 'Light' while MC at the best condition with 'Dark' is smaller than MC at the best condition with 'Light'. Since short-term memory under both conditions is enough for the NARMA10 prediction task, as mentioned already, the smaller $NMSE_{var.}$ of 'Dark' results from stronger nonlinearity than those of 'Light'. On 'Mix', although λ_{max} shows a relatively small value at a pulse interval of 15 ns as in cases of 'Dark' and 'Light', λ_{max} shows a large value at the interval of 15 ns, and λ_{max} at the best condition for NARMA10 is 4.09. In addition to a large MC of 32.08, this strong nonlinearity contributes to realizing the smallest $NMSE_{var.}$ of 0.163. Thus, the condition 'Mix', which is realized by visible light switching, breaks the trade-off relation between nonlinearity and MC. Figure 5(c) shows the return map of X_{12} and the phase portrait of X_{12} vs. X_7 under the best condition of the second-order nonlinear equation task. Both portraits show characteristic trajectories with different shapes for each period, as shown in Fig. 5(d), meaning that those trajectories are aperiodic. Thus, this trajectory proves strong nonlinearity (i.e., chaos) of the reservoir exhibiting positive λ_{max}. Figures 5(e) and (f) show NMSE and $NMSE_{var.}$ variations for the second-order nonlinear system and NARMA2 at various MC and λ_{max}. NMSE and $NMSE_{var.}$ at MC > 15 and λ_{max} < 1 are especially lower, and the distribution of NMSE is similar to that of $NMSE_{var.}$ due to similar required properties for these tasks. The lowest NMSE is at λ_{max} near 1. The distribution of $NMSE_{var.}$ for NARMA10 differs from those for other tasks[26]; the $NMSE_{var.}$ mainly depends on MC, as shown in Figs. 5(i) and (j). The tendency that $NMSE_{var.}$ reduces as MC increases shows NARMA10 strongly requires short-term memory property since this MC dependence of $NMSE_{var.}$ holds for all λ_{max}.

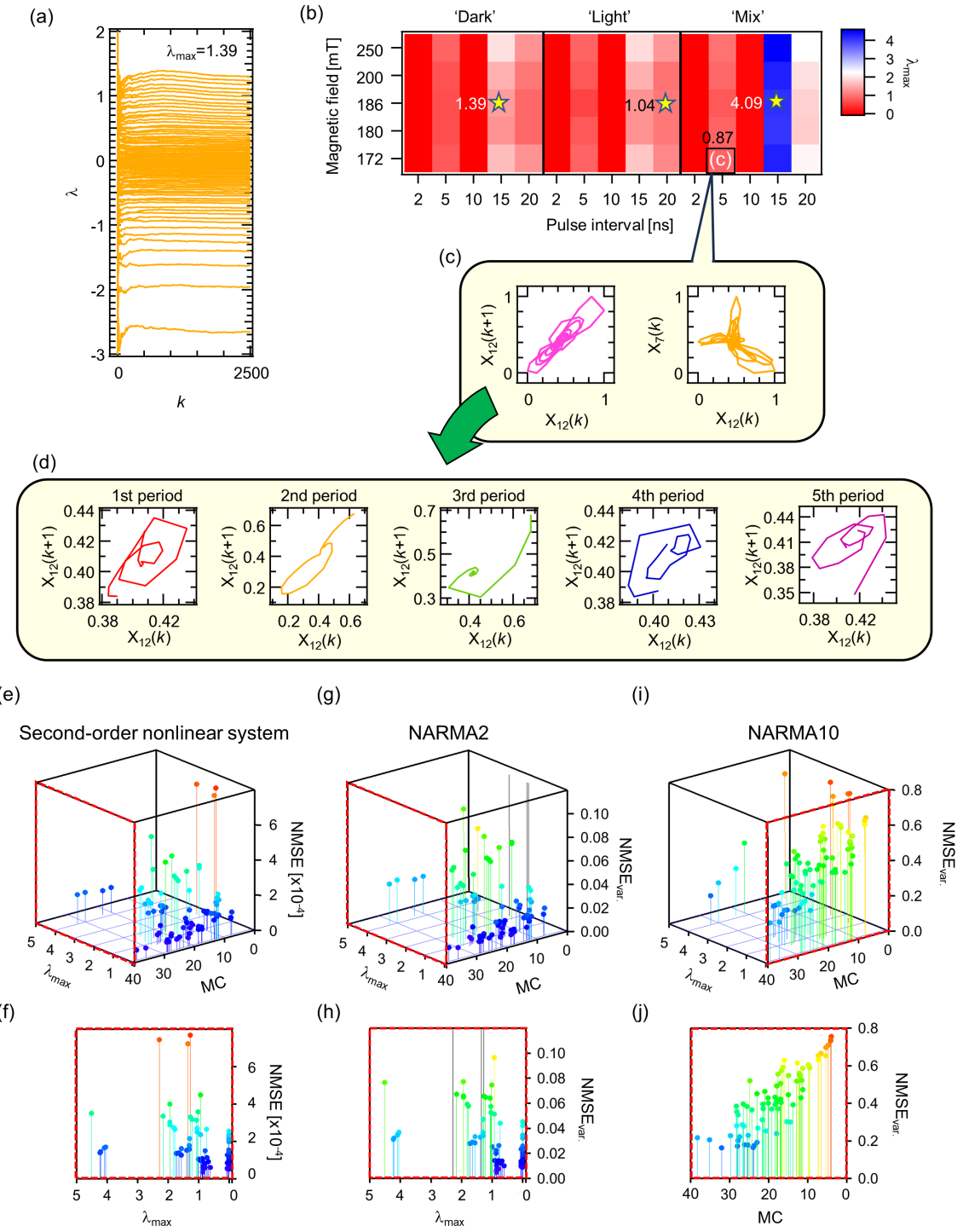

Fig. 5. (a) An example of Lyapunov spectra under the condition 'Dark', magnetic field of 186 mT, and pulse interval of 15 ns. (b) Maximum Lyapunov exponent (λ_{max}) variation at various magnetic fields and pulse intervals under the conditions (left) 'Dark', (middle) 'Light', and (right) 'Mix'. (c) Examples of return map of $X_{12}(k+1)$ versus $X_{12}(k)$ and phase portrait of $X_7(k)$ and $X_{12}(k)$ under the best condition for a second-order

nonlinear equation task. (d) return maps of $X_{12}(k+1)$ versus $X_{12}(k)$ from 1st to 5th periods. (e) λ_{max} and MC dependence of NMSE for a second-order nonlinear equation task. (f) λ_{max} dependence of NMSE. (g) λ_{max} and MC dependence of $NMSE_{var.}$ for a NARMA2 task. (h) λ_{max} dependence of $NMSE_{var.}$ (i) λ_{max} and MC dependence of $NMSE_{var.}$ for a NARMA10 task. (j) MC dependence of $NMSE_{var}$.

3.6. Micromagnetic simulation of the interfered spin wave with light switching

We performed a micromagnetic simulation of an interfered spin wave propagating under conditions 'Dark' and 'Light' to reveal the chaotic behavior of the interfered spin wave under the condition ‘Mix’. The pulse train of the magnetic field with a triangle shape was input to Exciter A and Exciter B to excite spin waves, and spin wave motion was monitored at the detector position (i.e., Detector A and Detector B), as shown in Fig. 6(a). The detected spin wave propagating under the condition ‘Light’ differs from that propagating under the condition 'Dark' due to M_s and H_a modulated by light irradiation. In addition to this, the detected spin wave motion at Detector A differs from that at Detector B. This result indicates that the multi-detection of spin waves leads to various signals being acquired and contributes to the higher dimensionality of the reservoir. As shown in the left and middle panels of Fig. 6(b), phase portraits of $X_1(k)$ versus $X_2(k)$ and $X_1(k)$ versus $X_4(k)$ under the condition ‘Dark’ have wide trajectories. This result indicates that the reservoir state obtained from the simulation result shows an aperiodic response that differs from period to period, meaning a chaotic state. The behavior of different trajectories for each period is shown in the right panel of Fig. 6(b). Such trajectories characterized as chaos were also observed in the simulation result under the condition ‘Light’, shown in Fig. 6(c), and the trajectory width was wider than 'Dark' one. This result means light irradiation enhances the instability of spin wave motion as time evolves. From Lyapunov spectra of simulated reservoir state with 100 nodes obtained from spin wave motion at Detector A and Detector B under the conditions 'Dark' and 'Light,' λ_{max} of ‘Mix’ was the positive value of 3.72, indicating chaos state as well as an experimental result.

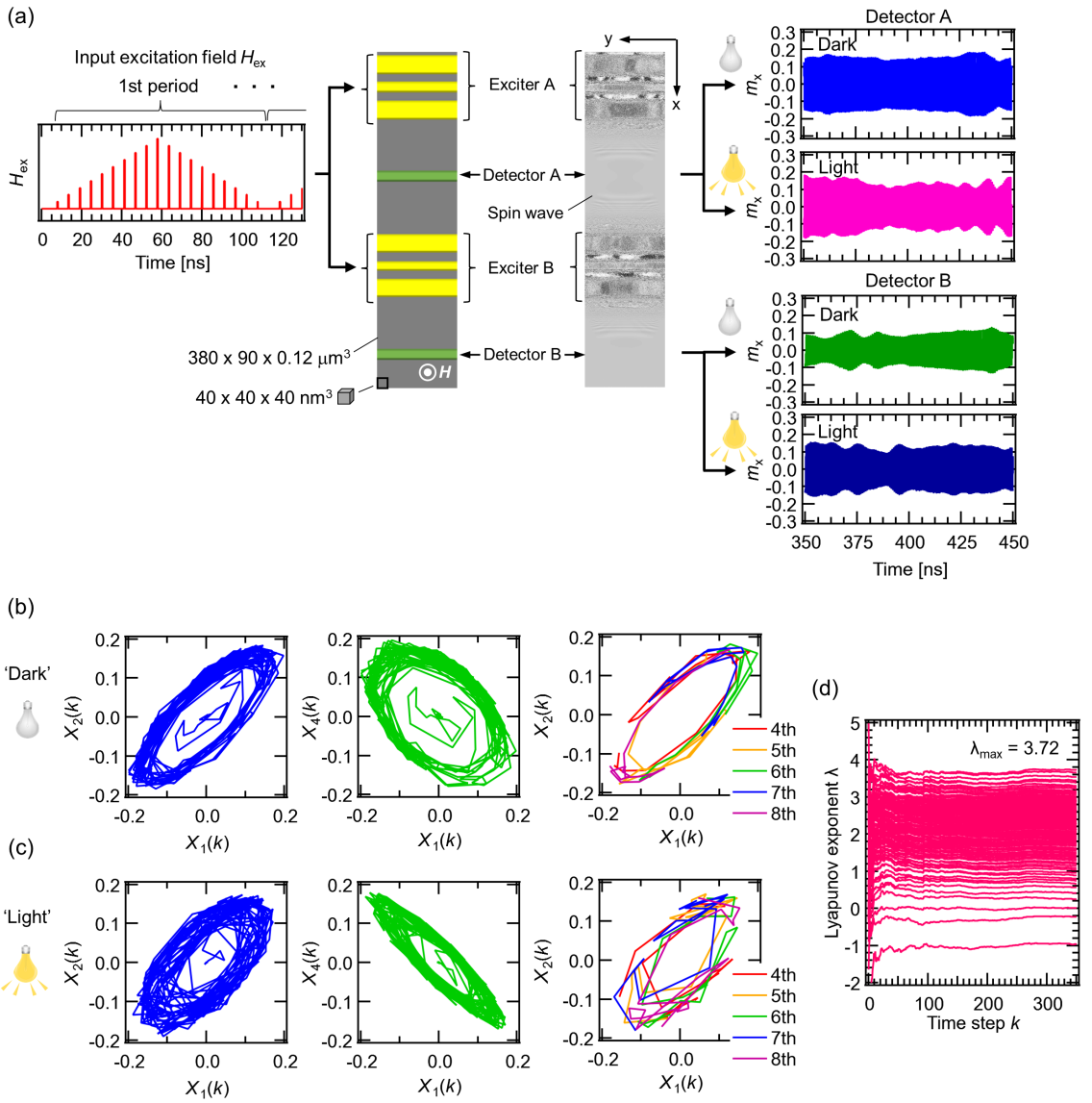

Fig. 6. (a) Simulation model of the nonlinear interfered spin wave with a waveguide of 380 x 90 x 0.12 μm^2 and calculated spin wave motion at Detector A and Detector B. The cubic mesh employed measured 40 nm x 40 nm x 40nm. The external magnetic field H is set to be applied perpendicularly to the surface of the waveguide. Pulsed triangle waves were input to Exciter A and Exciter B. x components of spin wave motions at Detector A and Detector B were monitored under 'Dark' and 'Light'. (b) Phase portraits of (left) $X_1(k)$ versus $X_2(k)$ and (middle) $X_1(k)$ versus $X_4(k)$ simulated under the condition 'Dark'. (right) phase portraits from 4th to 8th periods of $X_1(k)$ versus $X_2(k)$. (c) Phase portraits of (left) $X_1(k)$ versus $X_2(k)$ and (middle) $X_1(k)$ versus $X_4(k)$ simulated under the condition 'Light'. (right) phase portraits from 4th to 8th periods of $X_1(k)$ versus $X_2(k)$. (d) Lyapunov spectra of the interfered spin wave under the light switching.

3.7. Evaluation of complexity and entropy of reservoir state of the physical reservoir

Since chaos is not stochastic but complex behaviors, complexity and entropy were introduced to evaluate whether the feature of time-series data is complex or stochastic[[52],[53],[54],[55]]. Figures 7(a)-(e) show complexities C of the reservoir state of the 'Mix', simulated spin wave motions, and various time-series data as a function of permutation entropy H_e. There are minimum and maximum values of C (i.e., C_{min} and C_{max}). The position of the plot reflects the property of time-series data (i.e., randomness, noisiness, periodicity, and chaos) and provides visual support to determine said property. When H_e is 1.0 and C is 0.0, the signal is completely random (i.e., white noise), as shown in Fig. 7. Fractional Brownian motion is chromatic noise, which is a stochastic process[55], and its complexity C and entropy H_e depends on Hurst exponent H. C and H_e increases and decreases as H increases, as plotted in Fig. 7. It can be judged whether the behavior of time-series data is deterministic or stochastic since the curve drawn by these plots is an important indicator expressing a feature of time-series data. Concretely speaking, a signal is chaos (stochastic) when a plot is located above (below) the curve[55]. For example, C and H_e of the logistic map, which is known as a representative example of chaos, increases as coefficient r increases and is located above the curve of chromatic noise. The logistic map is described as follows,

$$f(t+1) = rf(t)(1-f(t)) \qquad (10).$$

Its behavior largely changes depending on parameter r. The logistic map is deterministic chaos by simple nonlinear mapping, and its C closes to maximum value when H_e is medium value, as shown in Fig. 7. If a signal shows periodic behavior, the combination of H_e and C is within the region of 0.1~0.2. If a signal shows a monotonically increment, said combination is 0.0. Furthermore, it was determined that the characteristics of the spin wave motion simulated in this study were chaotic since its combination of C and H_e was plotted near plots of the logistic map. As can be seen in Fig. 7, it was found to be independent of the position of the detector and the presence (i.e., 'Light') or absence ('Dark') of light irradiation. This result is consistent with drawing an attractor indicating chaos, shown in Figs. 6(b) and (c).

Based on the above relationship, we evaluated the characteristics of the reservoir state of the opto-magnonic reservoir under the condition 'Mix'. In the case of interval 2 ns shown in Fig. 7(a), a parabolic-shaped distribution of the plots can be seen regardless of detector position and light switching, and the combinations of C and H_e of all nodes were plotted in the chaos region. Therefore, it can be said that the dynamics seem to be chaos, which is supported by a positive λ_{max} of 8.61×10^{-5} shown in Fig. 5(b). It again varied at an interval of 10 ns, but as the interval lengthened, the plots were concentrated in a chaotic region, and the C decreased while H_e increased. The plots of interval 10 ns with small λ_{max}, which is 6.16×10^{-3} shown in Fig. 5(b), are parabolic-shaped distributions as well as those of interval 2 ns. Thus, the dynamics at intervals of 10 ns are also chaotic. On the other hand, the intervals 5 ns, 15 ns, and 20 ns, whose plots were concentrated, show relatively large positive λ_{max} of

0.87, 4.21, and 2.16, respectively. From Figs. 7(b), (d), and (e), the origin of large λ_{max} of 4.21 and 2.16 was the combination of relatively small C and H_e, while the small λ_{max} of 0.87 resulted from the combination of relatively large C and H_e. In particular, a part of the plots of the interval 15 ns, which shows the largest λ_{max} of 4.21, is distributed near the stochastic region. Note that this result does not indicate that the node state at the condition of interval 15 ns is stochastic. Thus, it was concluded that said chaotic state near the stochastic region is the optimal condition to achieve the highest computational performance in tasks where nonlinearity is emphasized, such as second-order nonlinear equation task (NMSE of 3.66×10^{-5}) and NARMA2 task ($NMSE_{var.}$ of 4.96×10^{-3}).

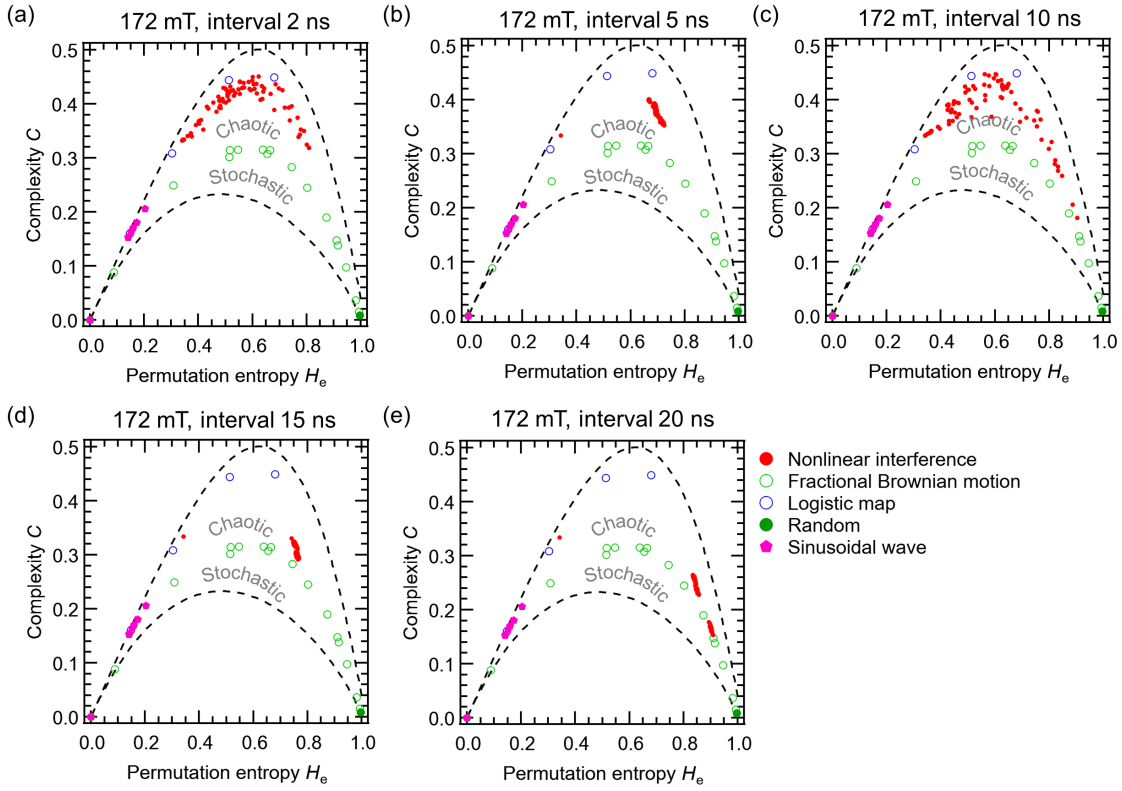

Fig. 7. Complexity C as a function of permutation entropy H_e under the conditions of 172 mT and (a) interval 2 ns, (b) interval 5 ns, (c) interval 10 ns, (d) interval 15 ns, and (e) interval 20 ns. Dashed lines represent minimum complexity C_{min} and maximum complexity C_{max}. Red plots represent complexities of reservoir states of the experimental nonlinear interfered spin waves. Plot at (0.341, 0.334) represents the complexity of triangle wave input to the opto-magnonic reservoir. Simulation 'Dark' and Simulation 'Light' represent the complexities of spin wave motions calculated using micromagnetic simulation assuming conditions of 'Dark' and 'Light'. Plots 'Fractional Brownian motion' represent complexities calculated with changing Hurst exponent H ranged [0, 1). Plots 'Logistic map' represent the complexity variation of the logistic map at various parameters r in its expression. r is ranged [3.0, 4.0]. Plot 'Random' represents the complexity of random wave ranging [0,1). Plots 'Sinusoidal wave' represents complexities of sinusoidal wave $\sin(2\pi ft)$, where $2\pi f$ and t are ranged [0.05, 5.00] and [0.00, 24.99], respectively. All sample length is 2500.

4. Conclusions

We developed reservoir computing with nonlinear interfered spin wave multi-detection by spin wave manipulation utilizing visible light irradiation. The opto-magnonic reservoir system in this study improved computational performance compared with a previous work utilizing nonlinear interfered spin wave multi-detection[26]. The diverse node states induced by visible light switching contribute to improving the ability to map time-series data in higher dimensional space through spin wave modulation. The crystal field transition occurred in two different Fe^{3+} sites of YIG by visible light switching, and spin wave property was modulated through decreases in both magnetization and magnetic anisotropy. NMSE for second-order nonlinear equation task and $NMSEs_{var.}$ for NARMA2 and NARMA10 were suppressed by 3.66×10^{-5}, 4.96×10^{-3}, and 0.163, respectively, and these values were lower than the nonlinear interfered spin wave multi-detection reservoir. This improvement in reservoir performance results from strong nonlinearity due to chaos, excellent short-term memory property with MC of 32.08, and the ability to map time-series data in higher dimensional space.

The reservoir computing utilizing spin wave interference modulated by visible light switching experimentally proved that utilizing different physical conditions is an effective way to improve the computational performance of the physical reservoir. The size of said reservoir system can be dramatically reduced by using ferromagnetic thin film in the future. Thus, high-performance artificial intelligence devices with compact volumes can be realized in the future. This scheme to improve reservoir performance through manipulating physical conditions can be applied to the physical reservoir utilizing any other physical dynamics based on magnetic property, electrical property, optical property, and so on.

References

1. H. Jaeger, H. Haas, H. Harnessing Nonlinearity: Predicting Chaotic Systems and Saving Energy in Wireless Communication. Science 304 (2004) 78-80.
2. W. Maass, T. Natschläger, H. Markram, Real-Time Computing without Stable States: A New Framework for Neural Computation based on Perturbations. Neural Comput. 14 (2002) 2531-2560.
3. D. Verstraeten, B. Schrauwen, M. D'Haene, D. Stroobandt, An Experimental Unification of Reservoir Computing Methods. Neural Netw. 20 (2007) 391-403.
4. G. Tanaka, T. Yamase, J. B. Héroux, R. Nakane, N. Kanazawa, S. Takeda, H. Numata, D. Nakano, A. Hirose, Recent advances in physical reservoir computing: A review. Neural Netw. 115 (2019) 100.
5. L. Appeltant, M. C. Sorano, G. van der Sande, J. Danckaert, S. Massar, J. Dambre, B. Schrauwen, C. R. Mirasso, I. Fischer, Information Processing using a Single Dynamical Node as Complex System. Nat. Commun. 2 (2011) 468.

6. L. Appeltant, G. van der Sande, J. Danckaert, I. Fischer, Constructing Optimized Binary Masks for Reservoir Computing with Delay Systems. Sci. Rep. 4 (2014) 3629.
7. C. Du, F. Cai, M. A. Zidan, W. Ma, S. H. Lee, W. D. Lu, Reservoir Computing using Dynamics Memristors for Temporal Information Processing. Nat. Commun. 8 (2017) 2204.
8. R. Midya, A. Wang, S. Asapu, X. Zhang, M. Rao, W. Song, Y. Zhuo, N. Upadhyay, Q. Xia, J. J. Yang, Reservoir Computing using Diffusive Memristors. Adv. Intel. Sys. 1 (2019) 1900084.
9. S. Kan, K. Nakajima, T. Asai, M. A. Kasaya, Physical Implementation of Reservoir Computing through Electrochemical Reaction. Adv. Sci. 9 (2022) 2104076.
10. S. Kan, K. Nakajima, T. Asai, M. A. Kasaya, Simple Reservoir Capitalizing on the Nonlinear Response of Materials: Theory and Physical Implementations. Phys. Rev. Appl. 15 (2021) 024030.
11. M. A. Kasaya, Y. Takeshima, S. Kan, K. Nakajima, T. Oya, T. Asai, Performance of Reservoir Computing in a Random Network of Single-walled Carbon Nanotubes Complexed with Polyoxometalate. Neuromorph. Comput. Eng. 2 (2022) 014003.
12. J. Torrejon, M. Riou, F. A. Araujo, S. Tsunegi, G. Khalsa, D. Querlioa, P. Bortolotti, V. Cros, K. Yakushiji, A. Fukushima, H. Kubota, S. Yuasa, M. D. Stiles, J. Grollier, Neuromorphic computing with nanoscale spintronic oscillators. Nature 547 (2017) 428.
13. W. Jiang, L. Chen, K. Zhou, L. Li, W. Fu, Y. Du, R. H. Liu, Physical Reservoir Computing using Magnetic Skyrmion Memristor and Spin Torque Nano-oscillator. Appl. Phys. Lett. 115 (2019) 192403.
14. N. Akashi, T. Yamaguchi, S. Tsunegi, T. Taniguchi, M. Nishida, R. Sakurai, Y. Wakao, K. Nakajima, Input-driven Bifurcations and Information Processing Capacity in Spintronics Reservoirs. Phys. Rev. Res. 2 (2020) 043303.
15. T. Kanao, H. Suto, K. Mizushima, H. Goto, T. Tanamoto, T. Nagasawa, Reservoir Computing on Spin-torque Oscillator Array. Phys. Rev. Appl. 12 (2019) 024052.
16. S. Tsunegi, T. Taniguchi, K. Nakajima, S. Miwa, K. Yakushiji, A. Fukushima, S. Yuasa, H. Kubota, Physical Reservoir Computing based on Spin Torque Oscillator with Forced Synchronization. Appl. Phys. Lett. 114 (2019) 164101.
17. T. Taniguchi, A. Ogihara, Y. Utsumi, S. Tsunegi, Spintronic Reservoir Computing without Driving Current or Magnetic Field. Sci. Rep. 12 (2022) 10627.
18. R. Nakane, G. Tanaka, A. Hirose, Reservoir Computing with Spin Waves Excited in a Garnet Film. IEEE Access 6 (2018) 4462-4469.
19. R. Nakane, A. Hirose, G. Tanaka, Spin Waves Propagating through a Stripe Magnetic Domain Structure and Their Applications to Reservoir Computing. Phys. Rev. Res. 3 (2021) 033243.
20. T. Ichimura, R. Nakane, G. Tanaka, A. Hirose, A Numerical Exploration of Signal Detector Arrangement in a Spin-wave Reservoir Computing Device. IEEE Access 9 (2021) 72637.
21. R. Nakane, A. Hirose, G. Tanaka, Performance Enhancement of a Spin-wave-based Reservoir Computing System Utilizing Different Physical Conditions. Phys. Rev. Appl. 109 (2023) 034047.

22. A. Papp, G. Csaba, W. Porod, Characterization of Nonlinear Spin-wave Interference by Reservoir-computing Metrics. Appl. Phys. Lett. 119 (2021) 112403.
23. S. Watt, M. Kostylev, A. B. Ustinov, Enhancing Computational Performance of a Spin-wave Reservoir Computer with Input Synchronization. J. Appl. Phys. 129 (2021) 044902.
24. S. Watt, M. Kostylev, Reservoir Computing Using a Spin-wave Delay-line Active-ring Resonator Based on Yttrium-iron-garnet Film. Phys. Rev. Appl. 13 (2020) 034057.
25. S. Watt, M. Kostylev, A. B. Ustinov, B. A. Kalinikos, Implementing a Magnonic Reservoir Computer Model Based on Time-delay Multiplexing. Phys. Rev. Appl. 15 (2021) 064060.
26. W. Namiki, D. Nishioka, Y. Yamaguchi, T. Tsuchiya, T. Higuchi, K. Terabe, Experimental Demonstration of High-performance Physical Reservoir Computing with Nonlinear Interfered Spin Wave Multi-detection. Adv. Intell. Syst. 5 (2023) 2300228.
27. I. T. Vidamour, C. Swindells, G. Venkat, P. W. Fry, A. Welbourne, R. M. Rowan-Robinson, D. Backes, F. Maccherozzi, S. S. Dhesi, E. Vasilaki, D. A. Allwood,, T. J. Hayward, Reconfigurable Reservoir Computing in a Magnetic Metameterial. Commun. Phys. 6 (2023) 230.
28. M. Nakajima, K. Tanaka, T. Hashimoto, Scalable Reservoir Computing on Coherent Linear Photonic Processor. Commun. Phys. 4 (2021) 20.
29. S. Sunada, A. Uchida, Photonic Reservoir Computing Based on Nonlinear Wave Dynamics at Microscale. Sci. Rep. 9 (2019) 19078.
30. T. Okumura, M. Tai, M. Ando, Experimental Study on Parallel and Analog Optical Reservoir Computing with Delayed Feedback System for Physical Implementation. Nonlinear Theory Appl. 10, (2019) 236-248.
31. Y. Paquot, F. Duport, A. Smerieri, J. Dambre, B. Schrauwen, M. Haelterman, S. Massar, Optoelectronic Reservoir Computing. Sci. Rep. 2 (2012) 287.
32. F. Duport, A. Smerieri, A. Akrout, M. Haelterman, S. Massar, Fully Analogue Photonic Reservoir Computer. Sci. Rep. 6 (2016) 22381.
33. Q. Vinckier, F. Duport, A. Smerieri, K. Vandoorne, P. Bienstman, M. Haelterman, S. Massar, High-performance Photonic Reservoir Computer Based on a Coherently Driven Passive Cavity. Optica 2 (2015) 438-446.
34. M. Hermans, P. Antonik, M. Haelterman, S. Massar, Embodiment of Learning in Electro-optical Signal Processors. Phys. Rev. Lett. 117 (2016) 128301.
35. K. Nakajima, H. Hauser, T. Li, R. Pfeifer, Information Processing via Physical Soft Body. Sci. Rep. 5 (2015) 10487.
36. S. G. Koh, H. Shima, Y. Naitoh, H. Akinaga, K. Kinoshita, Reservoir Computing with Dielectric Relaxation at an Electrode-ionic Liquid Interface. Sci. Rep. 12 (2022) 6958.

37. D. Nishioka, T. Tsuchiya, W. Namiki, M. Takayanagi, M. Imura, Y. Koide, T. Higuchi, K. Terabe, Edge-of-chaos Learning Achieved by Ion-electron-coupled Dynamics in an Ion-gating Reservoir. Sci. Adv. 8 (2022) eade1156.
38. T. Wada, D. Nishioka, W. Namiki, T. Tsuchiya, T. Higuchi, K. Terabe, A Redox-based Ion-gating Reservoir Utilizing Double Reservoir States in Drain and Gate Nonlinear Responses. Adv. Intell. Syst. 5 (2023) 2300123.
39. B. Barazani, G. Dion, J.-F. Morissette, L. Beaudoin, J. Sylvestre, Microfabricated Neuroaccelerometer: Integrating Sensing and Reservoir Computing in MEMS. J. Microelectromech. Sys. 29 (2020) 338-347.
40. J. C. Gartside, G. D. Stenning, A. Vanstone, H. H. Holder, D. M. Arroo, T. Dion, F. Caravelli, H. Kurebayashi, W. R. Branford, Reconfigurable Training and Reservoir Computing in an Artificial Spin-vortex Ice via Spin-wave Fingerprinting. Nat. Nanotech. 17 (2022) 460.
41. A. Welbourne, A. L. R. Levy, M. O. A. Ellis, H. Chen, M. J. Thompson, E. Vasilaki, D. A. Allwood, T. J. Hayward, Voltage-controlled superparamagnetic ensembles for low-power reservoir computing. Appl. Phys. Lett. 118 (2021) 202402.
42. S. H. Wang, G. Li, E. J. Guo, Y. Zhao, J. Y. Wang, L. K. Zou, H. Yan, J. W. Cai, Z. T. Zhang, M. Wang, Y. Y. Tian, X. L. Zheng, J. R. Sun, K. X. Jin, Strongly Extended Diffusion Length for the Nonequilibrium Magnons in $Y_3Fe_5O_{12}$ by Photoexcitation. Phys. Rev. Mat. 2 (2018) 051401.
43. G. B. Scott, D. E. Lacklison, J. L. Page, Absorption spectra of $Y_3Fe_5O_{12}$ (YIG) and $Y_3Ga_5O_{12}$: Fe^{3+}, Phys. Rev. B 10 (1974) 971.
44. S. H. Wemple, S. L. Blank, J. A. Seman, W. A. Biolsi, Optical properties of epitaxial iron garnet thin films, Phys. Rev. B 9 (1974) 2134.
45. A. Vansteenkiste, J. Leliaert, M. Dvornik, M. Helsen, F. Garcia-Sanchez, B. Van Waeyenberge, The design and verification of MuMax3. AIP Adv. 4 (2014) 107133.
46. T. Goto, T. Yoshimoto, B. Iwamoto, K. Shimada, C. A. Ross, K. Sekiguchi, A. B. Graovsky, Y. Nakamura, H. Uchida, M. Inoue, Three port logic gate using forward volume spin wave interference in a thin yttrium iron garnet film. Sci. Rep. 9 (2019) 16472.
47. M. A. Gilleo, S. Geller, Magnetic and Crystallographic Properties of Substituted Yttrium-IronGarnet, $3Y_2O_3{\cdot}xM_2O_3{\cdot}(5\text{-}x)Fe_2O_3$. Phys. Rev. 110 (1958) 73.
48. S. Khanra, A. Bhaumik, Y.D. Kolekar, P. Kahol, K. Ghosh, Structural and magnetic studies of $Y_3Fe_{5-5x}Mo_{5x}O_{12}$, J. Mag. Mag. Mater. 369 (2014) 14-22.
49. A. F. Atiya, New results on recurrent network training: Unifying the algorithms and accelerating convergence. IEEE Trans. Neural Networks 11 (2000) 697.
50. J. Y. Sarrion, Master's Thesis of Physics of Complex Systems at the University of Balearic Island (2019).
51. J. Hochstetter, R. Zhu, A. Lowffler, A. D. Alvarez, T. Nakayama, Z. Kuncic, Avalanches and edge-

of-chaos learning in neuromorphic nanowire networks. Nat. Commun. 12, (2021) 4008.
52. K. Fukuda, Y. Horio, Analysis of dynamics in chaotic neural network reservoirs: Time-series prediction tasks. Nonlinear Theory Appl. IEICE 12 (2021) 639.
53. R. López-Ruiz, H. L. Mancini, X. Calbe, Phys. Lett. A, 209 (1995) 321.
54. M. T. Martin, A. Plastino, O. A. Rosso, Physica A 369 (2006) 439.
55. O. A. Rosso, H. A. Larrondo, M. T. Martin, A. Plastino, M. A. Fuentes, Phys. Rev. Lett. 99 (2007) 154102.

CRediT authorship contribution statement

Wataru Namiki: Conceptualization, Methodology, Software, Investigation, Data Curation, Writing-Original Draft. **Yu Yamaguchi:** Investigation, Data Curation, Writing-Original Draft. **Daiki Nishioka:** Conceptualization, Methodology, Software. **Takashi Tsuchiya:** Conceptualization, Methodology, Writing-Original Draft, Project Administration, Funding Acquisition, Supervision. **Kazuya Terabe:** Writing-Reviewing and Editing, Project administration.

Acknowledgment

This work was in part supported by Innovative Science and Technology Initiative for Security Grant Number JPJ004596, ATLA, Japan. A part of this work was supported by Japan Society for the Promotion of Science (JSPS) KAKENHI Grant Numbers JP22KJ2799 (Grant-in-Aid for JSPS Fellows). A part of this work was supported by "Advanced Research Infrastructure for Materials and Nanotechnology in Japan (ARIM)" of the Ministry of Education, Culture, Sports, Science and Technology (MEXT). Proposal Number JPMXP1223NM5072. A part of this work was supported by NIMS Electron Microscopy Analysis Station, Nanostructural Characterization Group.